© 2019. Published by The Company of Biologists Ltd | Journal of Cell Science (2019) 132, jcs226753. doi:10.1242/jcs.226753

RESEARCH ARTICLE

Longer collagen fibers trigger multicellular streaming on soft substrates via enhanced forces and cell–cell cooperation

Bapi Sarker[1,*], Amrit Bagchi[1,*], Christopher Walter[2], José Almeida[2] and Amit Pathak[1,2,‡]

ABSTRACT

Grouped cells often leave large cell colonies in the form of narrow multicellular streams. However, it remains unknown how collective cell streaming exploits specific matrix properties, like stiffness and fiber length. It is also unclear how cellular forces, cell–cell adhesion and velocities are coordinated within streams. To independently tune stiffness and collagen fiber length, we developed new hydrogels and discovered invasion-like streaming of normal epithelial cells on soft substrates coated with long collagen fibers. Here, streams arise owing to a surge in cell velocities, forces, YAP activity and expression of mesenchymal marker proteins in regions of high-stress anisotropy. Coordinated velocities and symmetric distribution of tensile and compressive stresses support persistent stream growth. Stiff matrices diminish cell–cell adhesions, disrupt front–rear velocity coordination and do not promote sustained fiber-dependent streaming. Rac inhibition reduces cell elongation and cell–cell cooperation, resulting in a complete loss of streaming in all matrix conditions. Our results reveal a stiffness-modulated effect of collagen fiber length on collective cell streaming and unveil a biophysical mechanism of streaming governed by a delicate balance of enhanced forces, monolayer cohesion and cell–cell cooperation.

This article has an associated First Person interview with the first authors of the paper.

KEY WORDS: Collective cell migration, Epithelial cell, Matrix fiber, Mechanotransduction, Cell–cell adhesion, Matrix stiffness

INTRODUCTION

Collective cell migration in mechanically complex microenvironments is a fundamental biological process in tissue and organ morphogenesis, wound healing, angiogenesis and cancer progression (Mayor and Etienne-Manneville, 2016). On 2D surfaces, epithelial cells attain a sheet-like morphology and undergo collective migration (Nasrollahi et al., 2017; Zorn et al., 2015), with faster speeds on stiffer substrates (Nasrollahi and Pathak, 2016; Swartz et al., 2012), while maintaining broad leading edges. In contrast, grouped cells within fibrous 3D microenvironments escape large colonies in the form of narrow streams (Cheung et al., 2013, 2016; Dang et al., 2011; Elkhatib et al., 2017; Han et al., 2016; Riching et al., 2014), led by cells with upregulated expression of mesenchymal and mechanoactivation marker proteins (Friedl and Gilmour, 2009; Gaggioli et al., 2007). We do not yet understand whether this streaming mode of collective cell migration, compared to the broad leading edges in conventional monolayer migration, arises due to changes in dimensionality, microstructure or stiffness of the extracellular matrix (ECM). Previously, finger-like cell streams have been observed on 2D surfaces when epithelial monolayers were exposed to new surfaces via scratch wounds or lifting of barriers (Omelchenko et al., 2003; Poujade et al., 2007; Reffay et al., 2014, 2011), collagen gels (Yamaguchi et al., 2015) or artificially aligned topographies (Sharma et al., 2017). Instabilities at the leading edge have also been shown to cause finger-like projections in migrating monolayers of spindle-shaped endothelial cells, but not epithelial cells (Tambe et al., 2011). It is not yet known whether normal epithelial cells can exploit fiber architecture on soft substrates to undergo streaming. Furthermore, the biophysical mechanism of how cell streams arise in response to specific matrix properties remains unclear.

In this study, we ask the following question – can normal epithelial cells undergo cell streaming on soft substrates laden with long collagen fibers without any artificial alignment? If they can, the length of collagen fibers in the ECM will emerge as an important parameter that may independently regulate the modes of collective cell migration, even on soft substrates that are otherwise known to impede migration. Although cells are known to sense and respond to aligned structures, such as channel walls and aligned fibers (Nasrollahi and Pathak, 2016, 2017; Sharma et al., 2017), it is not known whether they respond to long versus short collagen fibers without their pre-alignment. We also interrogate whether substrate stiffness alters the influence of collagen fiber length on cell streaming, because stiff ECMs are known to enable aggressive invasion through enhanced epithelial–mesenchymal transition (EMT) and mechanoactivation (Lee et al., 2012; Leight et al., 2012; Wirtz et al., 2011; Zaman et al., 2006). These are important gaps in our knowledge about the streaming mode of collective cell migration, which grouped cells can efficiently exploit to escape an otherwise cohesive cell cohort to reach distant and narrow spaces within tissues. Addressing these questions remains a challenge because these matrix parameters – stiffness, dimensionality, fibrosity and ligand density – remain intimately intertwined in existing ECM scaffolds.

To isolate the effect of collagen fiber length independently of dimensionality, we conceived a flat substrate of defined stiffness on which collagen fibers could be tethered at varying length. Polyacrylamide (PA) hydrogels have enabled seminal mechanobiology studies during the past decade (Engler et al., 2006; Pelham and Wang, 1997), particularly owing to their tunable range of stiffness that mimics soft tissues (Discher et al., 2005). Collagen fibers buried under PA gels have been shown to influence broad changes in stem cell morphology, differentiation phenotype and gene expression (Dingal et al., 2015). However, conventional PA gels functionalized with the NHS-ester-based crosslinkers (e.g. sulfo-SANPAH) do not allow fiber formation in the collagen

[1]Department of Mechanical Engineering & Materials Science, Washington University, St Louis, MO 63130, USA. [2]Department of Biomedical Engineering, Washington University, St Louis, MO 63130, USA.
*These authors contributed equally to this work

‡Author for correspondence (pathaka@wustl.edu)

A.P., 0000-0003-4006-5119

Received 17 October 2018; Accepted 14 August 2019

Journal of Cell Science (2019) 132, jcs226753. doi:10.1242/jcs.226753

coating, which could be attributed to non-specific protein conjugation and a blockade of the lysine residues required for triple helix formation (Gurry et al., 2010; Lee et al., 2016; Mouw et al., 2014; Persikov et al., 2005). In native form, collagen has the ability to self-assemble into fibers, which has also been reported on rigid substrates (Elliott et al., 2003; McDaniel et al., 2007) but not on soft gels. In this study, we introduce aldehyde-functionalized PA gels (PAaf) that can support collagen fiber formation of varying length, tuned by the collagen incubation temperature (Doyle et al., 2015). Our hydrogel system of independently tunable stiffness and collagen fiber length presents a new material paradigm for deconstructing the influences of these two critical matrix parameters on modes of collective cell migration. Using this system, we reveal that long collagen fibers enable collective cell streaming at the leading edge, which, surprisingly, is more robust on the softer substrate. Through traction microscopy and velocity analyses, we show that collective streaming requires a delicate balance of cell–cell adhesion, force distribution and collective cooperation that can be disrupted by Rac inhibition or stiffer matrices. Our findings unveil a previously unknown ability of grouped cells to exploit long fiber architecture and undergo invasion-like streaming with enhanced mesenchymal and mechanoactivation markers. Importantly, the fiber length-dependent streaming prevails on soft substrates that are conventionally known to restrict cell migration and thus considered benign for cell invasion.

RESULTS

Pre-functionalized hydrogels with collagen tethering of varying fiber length

For functionalizing PA gels without the use of conventional post-hoc linkers, such as sulfo-SANPAH, we introduce active sites within the polymeric network of PA by co-polymerizing N-ethanal acrylamide (EA) with acrylamide and bis-acrylamide (Fig. 1A). Oxidation of N-hydroxyethyl acrylamide (HEA) through the agent pyridinium chlorochromate (PCC) generates primary aldehyde groups in HEA molecules and produces EA. Here, PCC is the Corey–Suggs reagent (Corey and Suggs, 1975) that has been shown to produce aldehydes by oxidizing primary alcohols at room temperature. The free aldehyde groups present in EA bind to the N-termini (ε-amino groups) of collagen by forming strong carbon-nitrogen double bonds (Schiff's base bond in Fig. 1A) (Sarker et al., 2014).

Through five different compositions, we show that our PAaf gels can vary from ∼0.3 kPa to ∼120 kPa in Young's modulus, as characterized by atomic force microscopy (Fig. 1B). For our cell migration studies, we used the acrylamide (A) and bis-acrylamide (B) ratios of 4% A:0.2% B and 12% A:0.6% B, which correspond to Young's moduli of 0.31±0.03 and 41.5±0.5 kPa (mean±s.d.), which we refer to as 'soft' and 'stiff', respectively. On these soft and stiff gels, we deposited a 0.05 mg/ml solution of collagen type I and incubated at 37°C temperature, which resulted in a collagen coating of short fibers (<2 µm), visualized by fluorescently labeled collagen-I, as shown in Fig. 1C,D. In comparison, standard PA gels functionalized by sulfo-SANPAH (i.e., without the EA), yield a patchy inhomogeneous collagen coating (Fig. S1A). Indeed, MCF10A cells form broken and discontinuous monolayers on conventional sulfo-SANPAH-treated PA gels compared to a continuous monolayer on PAaf gels (Fig. S1B). When the incubation temperature was reduced to 4°C, we found a 10-fold increase in the length of coated collagen fibers (>20 µm). Importantly, the collagen structure did not vary with gel stiffness, that is, our gels can tune stiffness and fiber length independently of one another. Fiber orientation analysis (Fig. S2A,B) shows a somewhat isotropic distribution of fiber angles on both soft and stiff gels, which indicates that fibers are not deposited in any preferred direction. The straightness factor of over 90% of the deposited fibers is above 0.8, which indicates that long fibers are continuous regardless of their orientation (Fig. S2C,D).

To assess the validity of our platform for varying collagen concentrations, we coated soft and stiff PAaf gels with sulfo-cyanine5 NHS ester dye-labeled 0.025 mg/ml and 0.1 mg/ml collagen solutions at both temperatures. As shown in Fig. S6, very low and high densities of collagen fibers are visible for 0.025 mg/ml and 0.1 mg/ml collagen-coated gels, respectively. Similar to the 0.05 mg/ml collagen coating, the collagen structure did not change with gel stiffness for other collagen concentrations. Collagen fibers density for the concentration of 0.05 mg/ml (Fig. 1C), which is used in all experiments in this manuscript, falls in middle of the collagen fiber densities that appeared for 0.025 mg/ml and 0.1 mg/ml of collagen, indicating that the protein-binding sites for both soft and stiff gels do not get saturated at these protein concentrations.

To understand the tethering of collagen fibers to soft and stiff gel surfaces, we analyzed rupturing of collagen fibers conjugated to PAaf gels using a previously established AFM-based methodology (Fuhrmann et al., 2008; Wen et al., 2014). We functionalized collagen-I antibody on the tip of an AFM cantilever probe and performed micro-indentation on the collagen fiber-coated PAaf gels, as illustrated in Fig. 1E and Fig. S5. As the AFM probe retracts from the gel surface, the collagen fiber unfolds and stretches until the antibody–protein bonds rupture. We analyzed the retraction force–displacement curves to identify rupture events and calculated forces and lengths associated each rupture of the collagen–PA gel bond (Fig. S5C,D). The number of ruptures per retraction event was higher for longer fibers, which are expected to be tethered to the PA surfaces in more locations (Fig. 1G). On stiffer gels, more ruptures are attributed to higher polymer density underneath the collagen fibers compared to what is found with softer gels (Fig. 1G). We found no significant difference in the stiffness of collagen fibers between their long and short configurations (Fig. 1F). Thus, cells likely respond to the PA gel stiffness and do not sense distinctions in longitudinal stiffness of long versus short fibers. We found that the average length between ruptures and the corresponding force did not appreciably change with fiber length or gel stiffness (Fig. S5C,D). Notably, the average rupture force was above 300 pN, which is over 2-fold higher than previously reported for sulfo-SANPAH-based crosslinking (Wen et al., 2014). Although a direct quantitative comparison may not be accurate across these two different material systems, our measurements indicate robust collagen fiber tethering across the four gel conditions.

Next, to assess whether this change in collagen fiber length alters cell morphology, we seeded MCF10A cells on soft PAaf gels of short or long fibers and acquired scanning electron microscopy (SEM) images of the front edge of a migrating MCF10A monolayer. We found a more-spread cell morphology in case of short collagen fibers (Fig. 1H). In contrast, the long fibers case resulted in elongated cell morphology with collagen fibers aligned along the cell. These images indicate that collagen fiber length could fundamentally alter the cellular response. In this manuscript, all studies are performed on four different substrate conditions corresponding to soft or stiff gels coated with long or short collagen fibers, which we denote as 'soft-short', 'soft-long', 'stiff-short' and 'stiff-long'.

Cell streaming enabled by longer collagen fibers on soft matrices

To investigate how collagen fiber length affects the collective cell response, we cultured monolayers of normal MCF10A mammary epithelial cells on the aforementioned PAaf gels. At the leading edge

Journal of Cell Science (2019) 132, jcs226753. doi:10.1242/jcs.226753

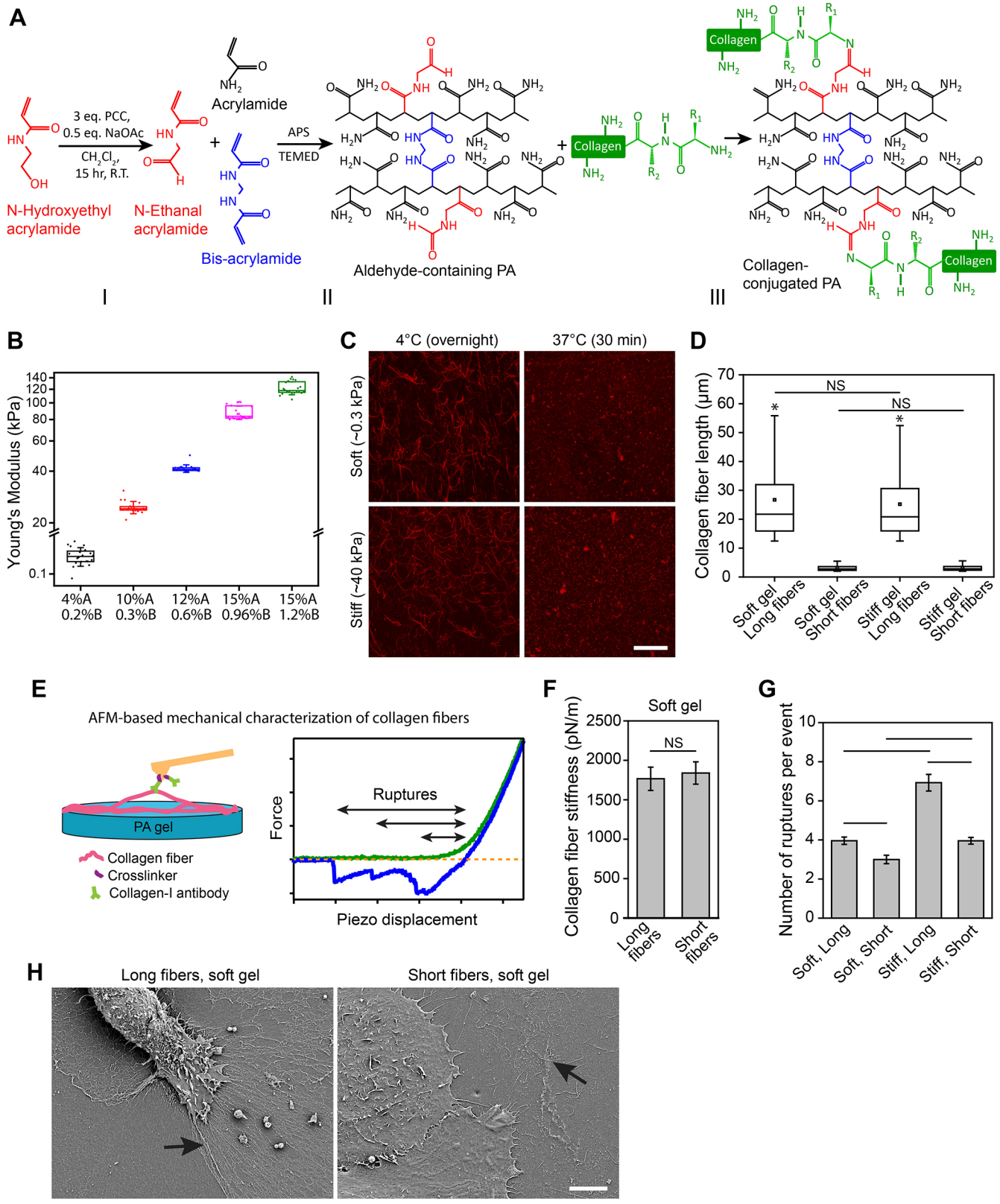

Fig. 1. See next page for legend.

of the migrating monolayer, we observed multicellular extensions of different shapes – some broad ones with short extensions out of the monolayer and some narrow ones with much longer outward extensions (Fig. 2A). To categorize these phenotypic differences, we calculated a ratio of length to average width of such collective extensions. We defined extensions of length-to-width ratios larger than three as 'streams' and smaller ones as 'blebs'. On gels with long fibers, we observed finger-like collective protrusions at the

Journal of Cell Science

Journal of Cell Science (2019) 132, jcs226753. doi:10.1242/jcs.226753

Fig. 1. Aldehyde-functionalized polyacrylamide hydrogels of tunable stiffness and collagen fiber coating. (A) Schematic of the reaction showing the steps for (I) oxidation of HEA and formation of N-ethanal acrylamide (EA), (II) copolymerization of EA with acrylamide and bis-acrylamide to synthesize aldehyde-containing PA (PAaf) network, and (III) conjugation of collagen to the PAaf gel. R.T., room temperature. (B) Young's moduli of PAaf gels with varying acrylamide and bis-acrylamide ratio. (C) Representative images of fluorescently labeled collagen type I on soft and stiff PAaf gels for varying incubation temperatures. Scale bar: 100 µm. (D) Length of collagen fibers on soft and stiff gels. For, B and D, the box represents the 25–75th percentiles, and the median is indicated by the line (the mean is indicated by the square in D). The whiskers show the 10–90th percentiles for B and D. **P*<0.05 between long and short fibers within the same stiffness. NS, not significant. (E) Schematic illustrating the interaction between a collagen-I antibody-functionalized AFM probe and the collagen-coated PAaf hydrogel in the force-spectroscopy study using AFM. A typical force–displacement curve is illustrated on the right, depicting approach (green), retraction (blue) and rupture lengths and indicating the distance of rupture points from the PAaf gel surface. (F) Stiffness of long and short collagen fiber tethered to soft PAaf gels (*n*=50). NS, not significant. (G) Average number of ruptures that occurred per retraction event when the collagen-I antibody-functionalized cantilever was retracted from gel surface during the protein-tethering study with AFM (*n*=100). Lines denote significant difference (*P*<0.05) in pairwise comparison. Data in F and G are presented as the mean±s.e.m. (G) SEM images of MCF10A cells at the leading edge of a migrating epithelial monolayer on soft gels coated with long or short fiber. Cell elongation along collagen fibers (denoted by arrows) in case of long fibers (left panel) and broad spreading on short fibers (right panel). Scale bar: 6 µm.

leading edge (Fig. 2B). Soft substrates had more fingers of higher length-to-width ratio (Fig. 2C,D), with more elongated individual cells (Fig. 2E,F). Strikingly, in the case of short fibers on both soft and stiff substrates, the leading edge of the colony remained stable without any finger-like structures. Instead, we noticed short and wide collective protrusions, termed as 'blebs' (Fig. 2B), with reduced elongation of individual cells (Fig. 2F). Although bleb-like protrusions at the leading edge have previously been observed in cell monolayer migration (Tambe et al., 2011), we report for the first time the formation of such long streams, over 300 µm, emanating from a colony of normal epithelial cells on a flat soft substrate coated with long collagen fibers. As a consequence of this aggressive streaming, we found that the 'soft-long' substrates caused over three times more cells to escape the monolayer compared to what was seen for the 'stiff-long' substrate (Fig. 2E). Surprisingly, the length of streaming and the number of escaped cells in the soft-long condition was higher than for stiff substrates, which are otherwise known to promote cell migration and monolayer instability. On both soft and stiff PA gels coated with short fibers, many fewer cells escaped from the monolayer.

Through particle image velocimetry (PIV), we found that cells within streams on soft-long substrates were twice as fast as those within the monolayer core (Fig. 2G,H). In comparison, on stiff-long substrates, higher cellular velocities were concentrated behind the stream (Fig. 2G). The occurrence of outwardly increasing velocity gradients exclusively on the soft-long substrates, which support streaming, indicates that acceleration of cells in the streams may be a key feature of persistent stream formation. We also found that order parameter and correlation length, over which velocity vector correlate with one another, were higher in case of longer fibers on soft gels (Fig. 2I–K). Despite overall higher cell velocities on stiff substrates, the effect of fiber length on order parameter and correlation length was much subdued compared to on the soft substrates (Fig. 2G–K). In sum, these results show that collagen fiber length can cause dramatic changes in collective migration phenotypes and the ability of cells to escape their larger cohorts, independently of matrix stiffness.

Longer fibers promote symmetric cellular tractions and monolayer stresses

We implemented the Fourier-transform traction microscopy, as described previously (Tambe et al., 2011, 2013; Trepat et al., 2009), performed calculation on soft gels, and found that average traction magnitudes on long fibers almost doubled compared to that on short fibers (Fig. 3A,B). On long fiber gels, which promote streaming, cellular tractions in the direction perpendicular to the emanating stream (T_y) segregate into two distinct regions of positive and negative tractions along the stream (Fig. 3A). From the tip of the stream to its base, the average normal stress is tensile in one half of the stream and compressive in the other half (Fig. 3C). These results indicate that, as the streams develop at the leading edge of the migrating monolayer, cells inside the streams deform the matrix symmetrically along the direction perpendicular to the stream, resulting in a bifurcation of positive and negative traction regions on the substrate. During this process, the cell monolayer develops compressive and tensile stresses in the two respective halves. The maximum shear stress is higher at the base of the stream, with a symmetric distribution, which indicates a systematic stress anisotropy in regions that cover stream and the base connecting it to the monolayer (Tambe et al., 2011). In comparison, on short fibers, the regions with positive and negative cellular tractions (both T_x and T_y) alternate with one another (Fig. 3A), without large regions of localized tensile or compressive stresses (Fig. 3C). Within the monolayer core, positive and negative tractions are homogeneously distributed. Tensile normal stresses at the leading edge on short fibers indicate that there is a concerted pulling effort of the cells in the direction of migration, which in turn maintains a stable leading edge. These results suggest that the ability of cells at the leading edge to generate higher forces and develop concentrated, yet symmetric, regions of monolayer stresses are the key mechanisms for the development of stable streams on soft substrates with long fibers.

Softer gels promote more persistent cell streaming

Although long collagen fibers promoted collective cell streaming on soft gels, it was surprising to find the loss of streaming on stiff gels (Fig. 2). Upon closer examination of streaming on soft versus stiff gels coated with long collagen fibers, we observed that multicellular streams ruptured due to dissociation of cells within the streams on stiff-long substrates. In comparison, the streams on soft-long substrates maintained their connection with the monolayer and grew over time. We further focused on cell velocity vectors in streams and examined the temporal evolution of their dis-alignment, quantified as $|\sin\theta|$, relative to the principal direction of all vectors within the developing stream. As shown in Fig. 4, on soft-long gels, velocity vectors stayed aligned along the stream for over 4.5 h. However, on stiff-long gels, we found that the dis-alignment of velocity vectors progressively grew worse over time, particularly at the base of the stream. As a result, after ∼3 h, the stream broke from the base, from the region with maximal dis-alignment (Fig. 4A). Consistent with these results on stiff-long substrates, the spatiotemporal kymographs of vector alignment, $\cos\theta$ relative to the principal direction of the stream, show a drop in the vector alignment after ∼2.5 h (dotted region in Fig. 4B). On soft-long gels, vectors remained aligned along the entire length of stream throughout the 4.5 h. At the final time-point, ∼90% of the total vectors were oriented between 0° and 18° along the principal direction of the stream on soft gel, showing that majority of the cells in the stream remain highly oriented along the stream (Fig. 4C). However, vectors in the streams on stiff-long gels were oriented

Journal of Cell Science (2019) 132, jcs226753. doi:10.1242/jcs.226753

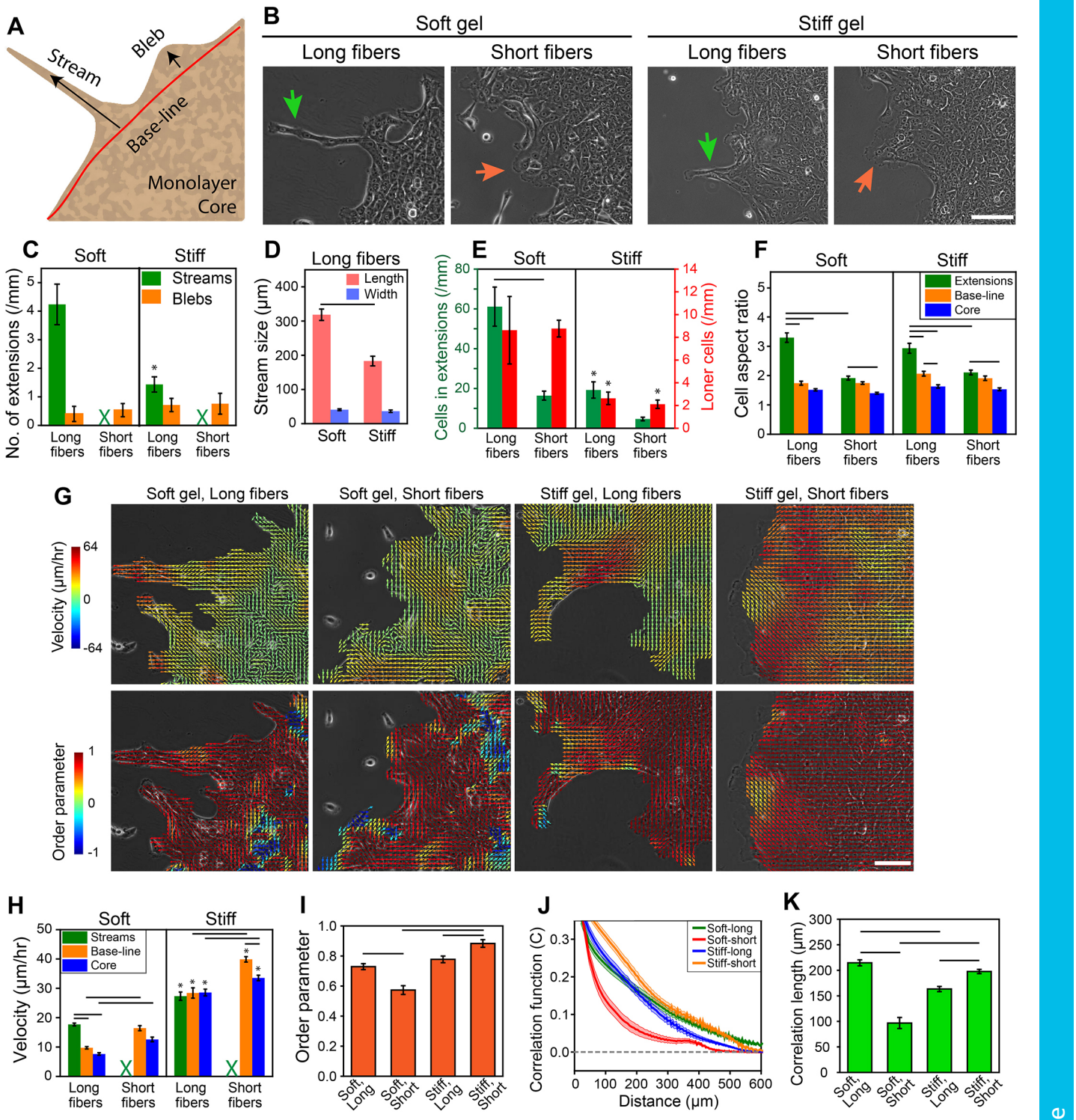

Fig. 2. Collective cell streaming and velocity coordination regulated by substrate stiffness and fiber length. (A) Schematic describing key regions of a migrating epithelial monolayer. (B) Representative images of leading edges of MCF10A cell monolayer on the four gel systems, where green and orange arrows indicate finger-like streams and blebs, respectively. Scale bar: 200 μm. (C) Average number of multicellular streams and protrusion blebs per unit length of base-line of the epithelial monolayer. (D) Length and width at the base of multicellular extensions, including both streams and blebs. (E) Average numbers of cells in the extensions, such as streams or blebs, per unit length of the base-line (green bars; *y*-axis on the left) and loner cells, that is, those detached from the monolayer, per unit length of the base-line (red bars; *y*-axis on the right). (F) Aspect ratio of cells in three different regions of the epithelial monolayer. (G) Velocity fields (top panel) and order parameter (bottom panel), obtained using PIV, with color coding of the leading edge of migrating epithelial monolayer on all four substrate conditions. Scale bar: 100 μm. (H) Average cell velocity in different regions of the monolayer. (I) Average order parameter calculated by including all visible regions of the monolayer. (J) Radial correlation curves for the cells in the extensions and the base of epithelial monolayer. (K) Average correlation lengths calculated from the correlation curves. Lines denote a significant difference (P<0.05) in pairwise comparison. Asterisks represent significant difference (P<0.05) between soft and stiff gels with same fiber length and same region of epithelial monolayer. Each correlation curve is a mean from 20 regions (10× field per region). Data are presented as the mean±s.e.m.

Journal of Cell Science (2019) 132, jcs226753. doi:10.1242/jcs.226753

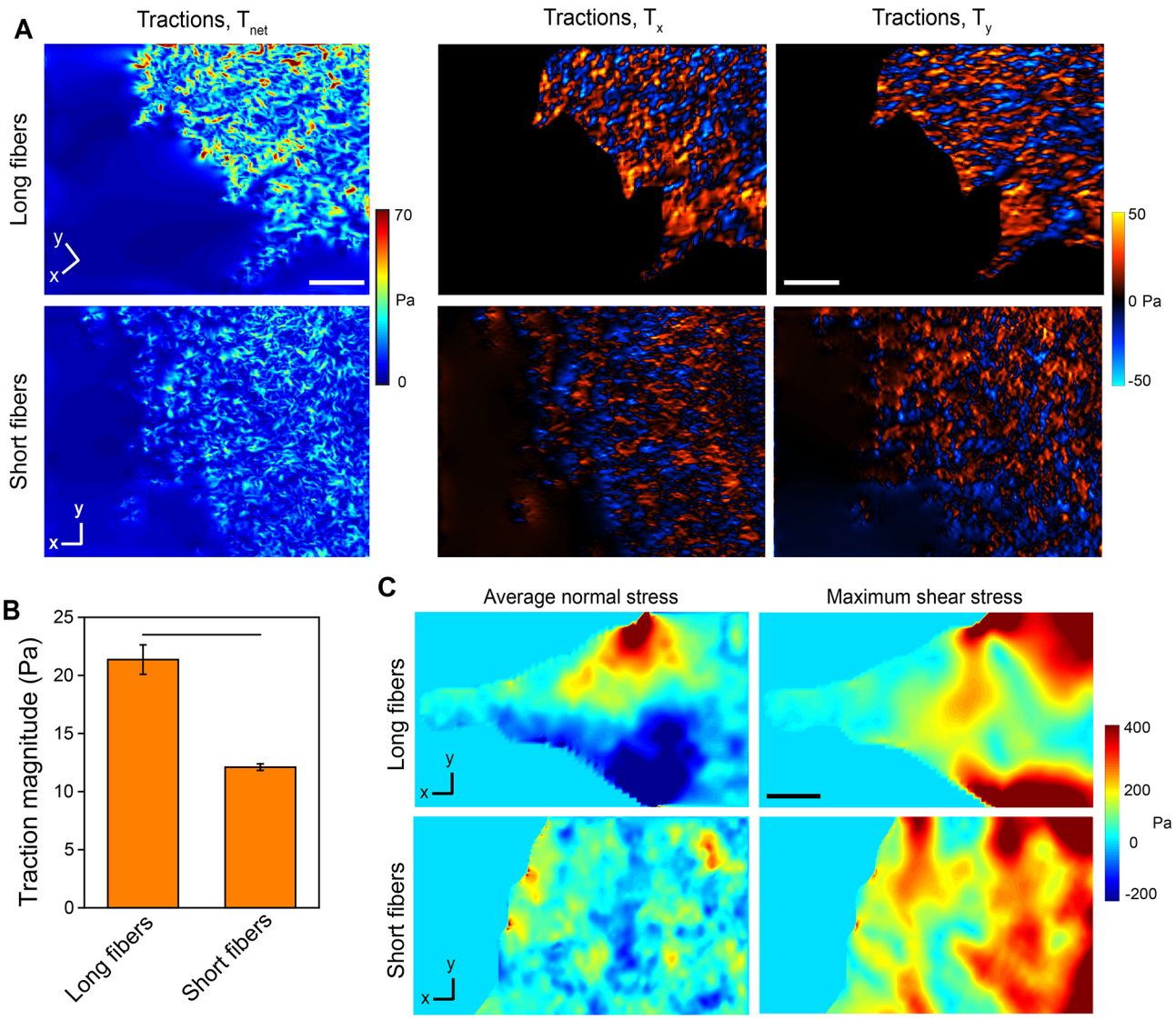

Fig. 3. Higher tractions in the monolayer front on long collagen fibers. (A) Maps of net cell–substrate tractions (T_{net}), tractions along the direction of streaming (T_x), and tractions in the direction perpendicular to streaming (T_y) on soft PAaf gels coated with long or short collagen fibers. Scale bars: 200 µm. (B) Average traction magnitude of epithelial monolayer on soft PAaf gels. n=10 regions. Data are presented as the mean±s.e.m. (C) Maps of average normal stress and maximum shear stress in the multicellular stream. Color codes are present on the right of each image. Scale bar: 100 µm.

evenly between 0° and 90°, indicating a loss of organized velocity alignment. Thus, the alignment of velocity vectors along the direction of nascent streams must persist over time for their conversion into long and stable streams, which occurs robustly on soft substrates but not on the stiff ones.

Upregulated mechanosensing markers in cell streams

Since the ability of cells to generate higher forces (Fig. 3) and migrate faster than the monolayer (Fig. 4) are key features of persistent streaming, we measured classic markers of cellular mechanoactivation by imaging (Fig. 5) for Yes-associated protein (YAP; also known as YAP1), an activator of the Hippo pathway (Dupont et al., 2011), and F-actin, responsible for protrusions (Rottner and Stradal, 2011). On both soft and stiff gels, longer collagen fibers caused an increase in F-actin expression, indicating higher stress fiber activity (Fig. 5D). Within the cell monolayer (core), nuclear YAP localization was higher on stiff gels (Fig. 5E), which is not surprising given that a reduction of cell density within monolayers has been shown to enable the stiffness-sensitive YAP response (Nasrollahi and Pathak, 2017). However, nuclear YAP increased towards the leading edge on all four substrates. Previously, it has been shown in standard cultures and wound-healing assays that cell density modulates YAP localization and phosphorylation (Zhao et al., 2007), with higher nuclear YAP and expression of Ki67, a cell proliferation marker, at the wound border. For the three substrate conditions that do not support stable cell streaming, that is, soft-short, stiff-long and stiff-short, the nuclear YAP location in the extensions (defined as either short streams or blebs) was 20–40% higher than in the core. However, on the soft-long substrate that supports robust streaming, the nuclear YAP for cells within the streams was over 250% higher than in the monolayer core. Such a drastic gradient in cellular mechanoactivation, going from the monolayer core to the stream, may be the cause of instabilities at the leading edge that promote cellular streaming. Notably, the streaming cells on soft substrates with long fibers show nuclear YAP levels that are similar to those of the stiff gels. This is a

Journal of Cell Science (2019) 132, jcs226753. doi:10.1242/jcs.226753

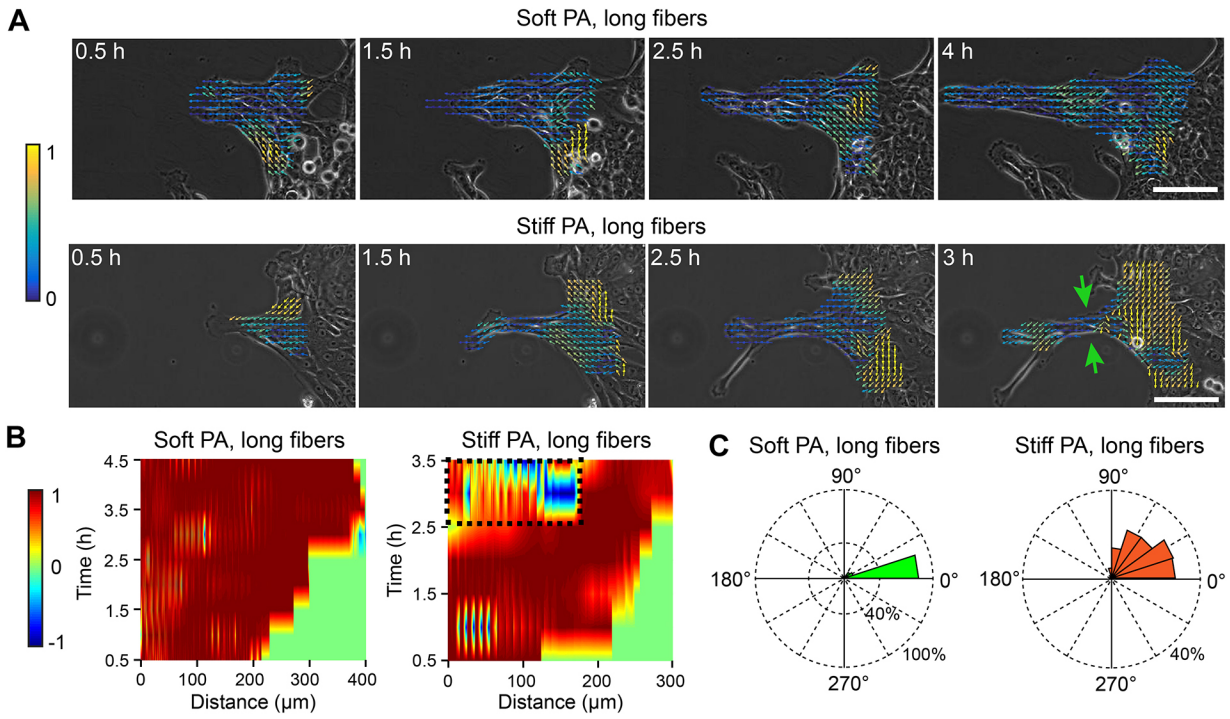

Fig. 4. Persistent velocity alignment and streaming on soft substrates with long fibers. (A) Color-coded velocity vectors showing alignment along the principal direction of the stream. Alignment is measured as |sinθ| between individual velocity vectors and the principal vector. Maximum alignment and dis-alignment are indicated by blue and yellow, respectively. Green arrows show the breaking point of the stream. Scale bars: 100 µm. (B) Position–time kymographs of velocity components, according to the color code, along the principal direction of the stream ($v\cos\theta$). The dashed box in the right-hand image represents the region of maximum dis-alignment. (C) Rose-plots of velocity vectors alignment (angles in degrees) along the principal direction of the stream.

surprising result because conventionally, soft matrices cause cytoplasmic localization of YAP by inhibiting nuclear YAP transport (Elosegui-Artola et al., 2017). Thus, the collagen architecture of longer fibers can enhance cellular mechanoactivation independently of matrix stiffness.

For persistent and stable streaming, in contrast to the breakage of streams observed on stiff substrates (Fig. 4), the cells with higher mechanoactivation at the leading edge should maintain cohesivity with the monolayer at large. In other words, while the streaming cells enhance their mechanoactivation, which is expected to trigger expression of mesenchymal marker proteins, the cell–cell adhesions should maintain their physical connection with the monolayer. To investigate these possibilities, we stained and imaged for vimentin, a mesenchymal marker, and the cell junction protein E-cadherin (E-cad), an epithelial marker. Through western blotting, we found that the total (cytoplasmic and junctional) expression of E-cad was fairly consistent across the four matrix conditions, with a slight reduction on stiff matrices (Fig. S4B). To assess cell–cell adhesions and cooperation, we measured E-cad localized at the cell membrane. On stiff gels, the vimentin expression increased, and membrane localization of E-cad decreased (Fig. 5C,F,G), both of which are consistent with the stiffness-dependent EMT observed previously (Brown et al., 2013; Nasrollahi and Pathak, 2016; Pathak, 2016; Walter et al., 2018; Wei et al., 2015). On soft gels, longer collagen fibers promoted vimentin expression (Fig. 5F), which suggests an upregulation of mesenchymal traits in conjunction with enhanced mechanoactivation (Fig. 5E). However, the cells within the streams on soft-long substrates maintained high levels of E-cad localization at cell–cell junctions (Fig. 5G), which suggests that cell–cell cohesion and cooperation is maintained during streaming despite an enhanced cellular mechanoactivation.

Cell–cell cooperation and collective streaming is disabled upon Rac1 inhibition

We have now shown that the ability of cells to migrate in a coordinated fashion (Fig. 2), to maintain their velocity orientation along the stream (Fig. 4), and the preservation of cooperation via cell–cell adhesions (Fig. 5) are critical features of cell streaming on soft-long substrates. To test whether direct inhibition of communication across cadherin-based cell–cell junctions also disrupts streaming, we treated cells with EGTA, a Ca^{2+} chelation agent, and found no stream-like processes (Fig. S7). Thus, the absence of cell–cell adhesions precludes any semblance of streaming or other forms of cohesive collective cell migration. Since Rac1, a member of the Rho family of GTPases, is known to fundamentally regulate cell polarization and cell–cell adhesions (Ehrlich et al., 2002; Mack et al., 2011), we asked whether its disruption could affect cell streaming. We chose Rac1 as a target because it is expected to disrupt cell–cell coordination without direct dissociation of cell–cell adhesions. Indeed, after Rac1 inhibition, we found no stable or consistent finger-like streams at the leading edge (Fig. 6A). In case of long fibers, we found larger number of single cells leaving the monolayer (Fig. S4), indicating a loss of cell–cell cohesion.

Although nuclear YAP localization did not significantly change on stiff gels after Rac1 inhibition, the difference between long and short fibers reduced on soft gels (Fig. 6B) compared to the untreated cells. Most notably, we found that cell elongation reduced dramatically on both soft and stiff gels coated with long fibers (Fig. 6E), which suggests that Rac1 plays a critical role in allowing the cells to morphologically align along the developing streams on substrates with longer fibers. We also found that the vimentin expression on the soft-long substrates increased compared to

Journal of Cell Science (2019) 132, jcs226753. doi:10.1242/jcs.226753

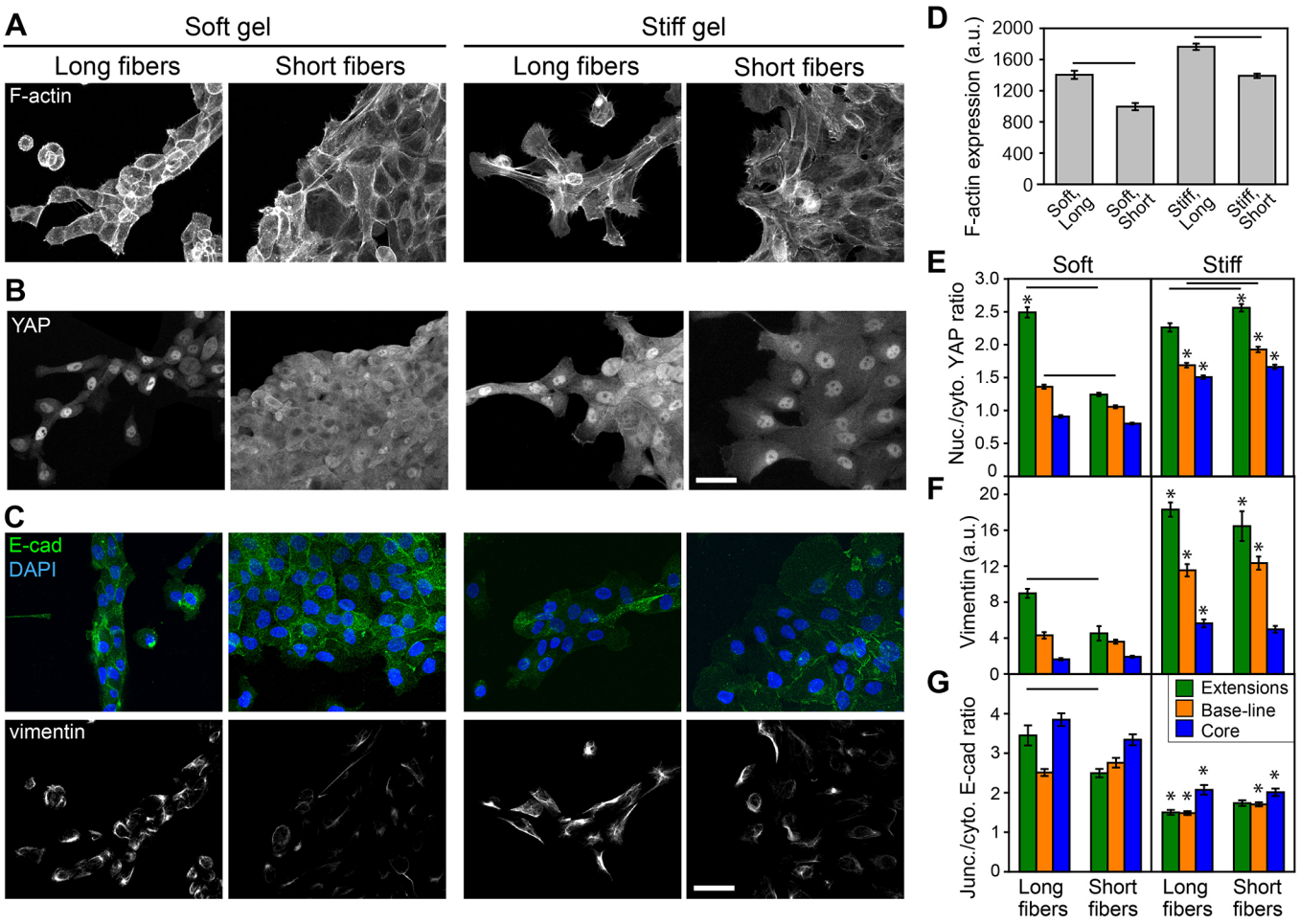

Fig. 5. Enhanced cell mechanosensing markers in collective cell streams. Immunofluorescence images of (A) F-actin, (B) YAP, and (C) E-cad, DAPI and vimentin. Scale bars: 50 µm. (D) Mean integrated fluorescence intensity of F-actin per unit area of cells within streams or blebs. (E) Mean nuclear-to-cytoplasmic ratio of YAP fluorescence intensity, (F) mean integrated vimentin fluorescence intensity per cell, and (G) mean junctional-to-cytoplasmic E-cad fluorescence intensity of cells in three different regions of the monolayer. Lines denote significant difference (P<0.05) in pairwise comparison. Asterisks represent significant difference (P<0.05) between soft and stiff gels with same fiber length and region of epithelial monolayer. Averages were calculated by analyzing at least 100 cells per condition for YAP expression, 20 cells per condition for F-actin expression and 10 images per condition for vimentin expression. Data are presented as the mean±s.e.m.

untreated cells (Fig. 6C), indicating a rise in mesenchymal signatures and loss of the cell–cell cohesivity that is required for stable streaming. To further confirm the change in vimentin expression after Rac1 inhibition, we performed western blotting. On soft gels, vimentin expression increased for both long and short collagen fiber conditions after Rac1 inhibition (Fig. S4B), consistent with the outcomes from immunofluorescence staining (Fig. 6C). On stiff gels after Rac1 inhibition, both immunofluorescence (Fig. 6C) and western blot (Fig. S4B) data show a reduction in vimentin expression.

Through velocimetry analyses, we found a significant reduction in cell velocity on stiff substrates regardless of fiber length (Fig. 6G), resulting in values closer to those on soft substrates. Importantly, the order parameter and correlation length significantly reduced on soft-long substrates (Fig. 6H–J), which coincides with the loss of cell elongation and rise of vimentin expression. Notably, the order parameter distribution was more heterogeneous for Rac1-inhibited cells in all conditions (Fig. 6F) compared to the untreated cells (Fig. 2G), with a significant reduction in the base region of the leading edge. These results show that Rac inhibition fundamentally abrogates the ability of cells to elongate, coordinate their velocities and maintain cell–cell cohesion, particularly on soft-long substrates, resulting in a complete loss of collective cell streaming.

DISCUSSION

Here, we present a new hydrogel system that allows independent control over substrate stiffness and the length of coated collagen fiber. By using this system, we have shown that collagen fiber length can fundamentally alter collective cell migration phenotypes. Conventionally, soft matrices reduce cell migration speeds, normal epithelial cells are highly cohesive and form structurally stable boundaries, and flat substrates allow sheet-like migration (Nasrollahi et al., 2017; Sunyer et al., 2016; Tambe et al., 2011). Our findings show that just by using long collagen fibers, as opposed to the standard fibrillar collagen coating, grouped cells at the leading edge of a normal epithelial monolayer on soft flat substrates acquire enhanced mechanoactivation and form long streams. Previously, such persistent and lengthy collective cell streaming had more commonly been observed in 3D environments (Clark and Vignjevic, 2015; Leung et al., 2017). Our results unveil an important role that collagen fiber length plays in dictating

Journal of Cell Science (2019) 132, jcs226753. doi:10.1242/jcs.226753

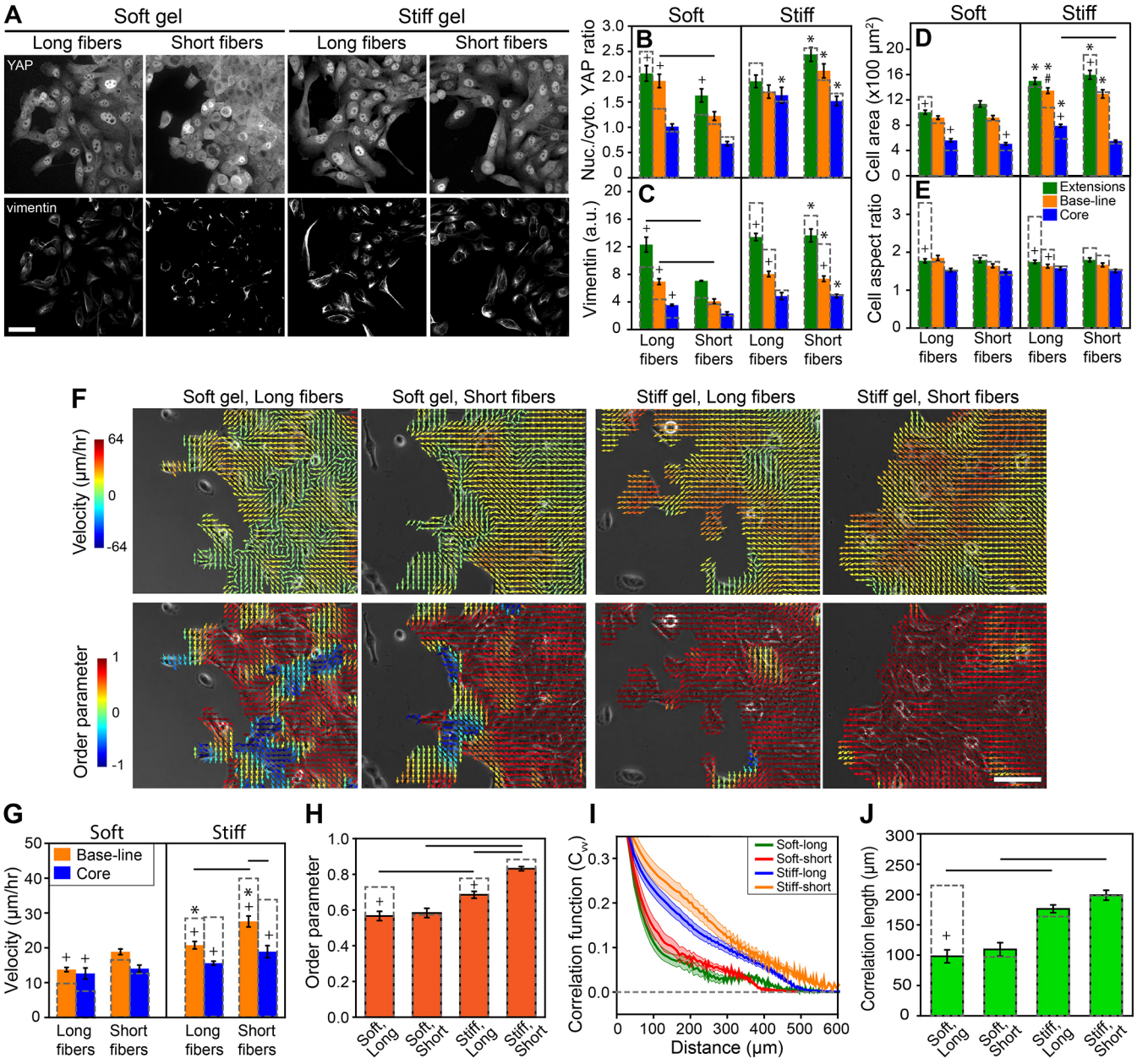

Fig. 6. Rac1 inhibition restricts stream formation through reduced cell elongation and cell–cell cooperation. (A) Immunofluorescence images of YAP and vimentin in MCF10A cells after Rac1 inhibition. Scale bar: 50 µm. Average (B) nuclear-to-cytoplasmic ratio of YAP fluorescence intensity, (C) integrated vimentin fluorescence intensity per cell, (D) cell area, and (E) aspect ratio of cells in three different regions of the epithelial monolayer. (F) Color-coded velocity fields (top panel) and order parameter (bottom panel), obtained using PIV. Scale bar: 100 µm. (G) Average velocity in different regions of the monolayer. (H) Average order parameter calculated by including all visible regions of the monolayer. (I) Radial correlation curves for the cells at the extensions and base. (J) Average correlation lengths calculated from the correlation curves. Lines denote significant difference (P<0.05) in pairwise comparison. Asterisks represent significant difference (P<0.05) between soft and stiff gels with same fiber length and region of the monolayer. Plus symbols denote significant difference (P<0.05) compared to the wild-type (untreated) condition. The bars shown with the gray dashed outline represent corresponding values for wild-type (untreated) cells. Each correlation curve is a mean from 10 regions (10× field per region). Data are presented as the mean±s.e.m.

grouped cell cohesion and migration behavior. One alternative hypothesis that emerged is that cells might be responding to the longitudinal stiffness of longer collagen fiber, not necessarily their length. Through force spectroscopy of collagen fibers (Fig. 1E), we found that both long and short fibers were robustly tethered to the gel surface and had similar longitudinal stiffness properties (Fig. 1F,G). As a result, when cells pull on either long or short fibers, they sense the PA gel stiffness, not necessarily the longitudinal stiffness of either short or long collagen fibers. Thus, both short and long fibers are likely to provide similar ‘stiffness signals’ to the cells for a given PA gel stiffness.

Another possibility is that as cells respond to long collagen fibers, they might also sense a signal of high ligand density through the collagen length. Thus, the phenomenon of haptotaxis, in which cells move toward higher ligand density, might be intimately tied to the mechanism of contact guidance that is conventionally invoked to understand cell migration along collagen fibers and aligned structures. In our material system, both long and short collagen

Journal of Cell Science (2019) 132, jcs226753. doi:10.1242/jcs.226753

fibers were found to be robustly tethered on top of compliant 2D hydrogels (Fig. 1; Fig. S5), but we observed streaming only in case of long fibers. Although stiff gels did not promote sustained streaming due to a loss of cell–cell cooperation (Fig. 4), cells on long fibers did commence streaming in both soft and stiff gels. Since both long and short fibers provide robust ligand density, but only long fibers promote streaming, it is likely that contact guidance plays a bigger role than haptotaxis in cell streaming. Importantly, since both the rupture force and the longitudinal stiffness of collagen fibers did not vary with gel conditions, it is likely that the operative mechanism for streaming is governed by the ability of cells to sense fiber length and gel stiffness, not necessarily fiber stiffness and ligand density.

Based on the ability of cells to interact with collagen fibers, we anticipated early on that altering the collagen fiber length would affect the cell population response. However, the extent of robust cell streaming on soft substrates was somewhat unexpected, particularly given that soft gels otherwise limit cell migration. Even more surprising was the finding that the stiff substrates with long collagen fibers did not support persistent streaming, despite higher cellular mechanoactivation and levels of EMT marker proteins. By analyzing velocity correlations, substrate traction, monolayer stress and the levels of mechanoactivation markers, we showed that although steep spatial gradients of velocity and mechanoactivation near the migrating leading edge are essential for the initiation of a stream, it must be sustained by velocity coordination and cell–cell cooperation over length and time for robust streaming (Fig. 7). In other words, while a controlled instability at the leading edge is good for streaming, it cannot survive without preserving a delicate balance of forces, cell–cell adhesions and ordered velocities. Indeed, despite having high levels of mechanoactivation markers, cells within streams show high E-cad expression at cell–cell adhesions, which is consistent with previous findings of the maintenance of cell–cell contacts between leaders and followers during collective cell migration (Poujade et al., 2007). The preservation of junctional E-cad within the cells on soft gels with long fibers enables intercellular cooperation and assists in collective streaming. In our experiments, stiff substrates enable homogeneously fast migration over the entire leading edge, which in turn reduces the possibility of such sudden gradients and instabilities at the leading edge. When some streams do form on stiff substrates with long fibers, the chaotic nature of the velocity vectors breaks those streams. It is possible that the rise in both the stiffness and the fiber length provide two additive inputs for enhanced migration, which in turn disrupt the balance of faster cells along with the cell–cell cohesion and cooperation required for streaming. Separately, Rac1 inhibition disables cell elongation and cell–cell cooperation. It is conceivable that although long collagen fibers attempt to guide the Rac-inhibited cells, the lack of persistent protrusions and weak cell–cell cooperation with the leader cells disable the formation of stable streams. Thus, collective cell streaming can be hampered by either mechanical or biochemical factors, albeit via different mechanisms.

Our work posits a biophysical mechanism for the formation of invasion-like multicellular streams that relies on a delicate balance of cellular mechanoactivation and cell–cell cooperation that can be fundamentally altered by collagen fiber length, which goes beyond the known role of matrix stiffness in mechanosensitive cell migration. These mechanisms of matrix architecture-dependent cell streaming may have profound implications for morphogenesis, regeneration, wound repair and tumor invasion, in which cells move collectively through environments that are soft, stiff, gelatinous, fibrous, 2D, 3D or anywhere in between. Beyond this work, our novel PAaf gel system will improve protein attachment, without the use of post-hoc cross-linkers, for wide-ranging cell mechanobiology studies.

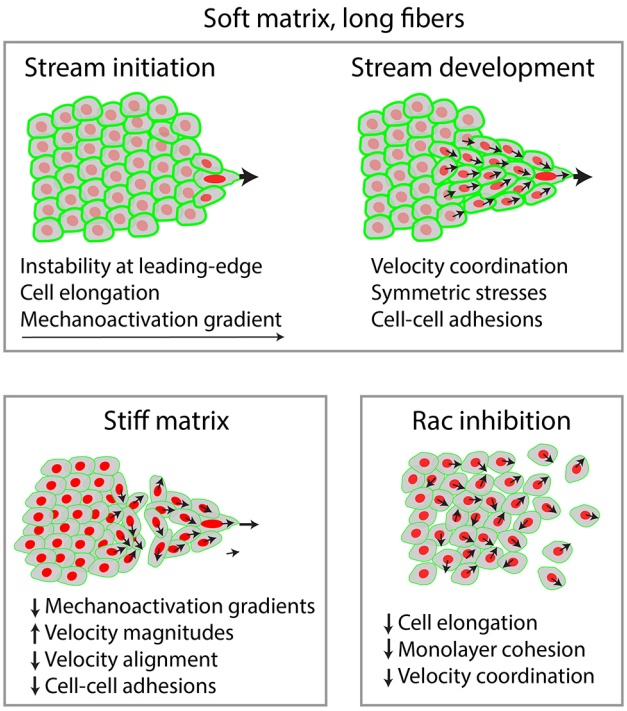

Fig. 7. Schematic description of collective cell streaming due to a balance of cellular mechanoactivation and cell–cell cooperation. On soft gels with long fibers, cells generate forces and alignment for collective streaming while maintaining some cell–cell adhesions. Increased stiffness reduces cell–cell cohesion and Rac1 inhibition disrupts cellular coordination and elongation, both of which disrupt collective streaming.

MATERIALS AND METHODS

Oxidation of alcohol to aldehyde

N-hydroxyethyl acrylamide (HEA) was oxidized using pyridinium chlorochromate (PCC) to generate primary aldehyde groups in HEA molecules. To perform the oxidation reaction, 30 ml of anhydrous dichloromethane (EMD; Millipore) was taken in a 250 ml round-bottom flask, to which 1.15 g of HEA (Sigma-Aldrich) was added. Approximately three equivalents (3.23 g) of solid PCC (Acros organics) were added to the 0.2 M solution of the alcohol in anhydrous dichloromethane. Then, 5 g of Celite® (Thermo Fisher Scientific) was added to the mixture as a solid support so that the reduced chromium salts could deposit over Celite® solid particles and easily be removed by filtration. Moreover, in order to moderate the acidity of PCC, 0.615 g (7.5 mmol) of anhydrous sodium acetate (Thermo Fisher Scientific) was added and the resulting reaction mixture was stirred at room temperature for 15 h in the dark. Then the mixture was filtered, and the collected organic phase was concentrated in a round-bottom flask, giving a crude aldehyde, N-ethanal acrylamide (EA).

Synthesis of aldehyde-functionalized polyacrylamide hydrogels and collagen coating

Polyacrylamide (PA) gels were chemically modified by incorporating synthesized EA to facilitate protein conjugation. Aldehyde-functionalized polyacrylamide (PAaf) gels with the desired stiffness were fabricated on a glass coverslip (diameter 15 mm, Thermo Fisher Scientific). PA precursor solutions were prepared by mixing varying amounts of acrylamide (A, Bio-Rad) and bis-acrylamide (B, Bio-Rad) according to the previous stiffness characterization of PA gels as the monomer (A):crosslinker (B) percentages of 4% A:0.075% B, 4% A:0.2% B, 10% A:0.3% B, 12% A:0.6% B, 15%

A:0.96% B and 15% A:1.2% B (Saha et al., 2008; Ulrich et al., 2009). EA was added to the PA gel precursor mixtures at a volume ratio of 1:75 (EA: acrylamide). To initiate polymerization, 0.5% ammonium persulfate (APS, Sigma-Aldrich) and 0.05% tetramethylethylenediamine (TEMED, Sigma-Aldrich) were added to the precursor mixtures. Then, 35 µl of gel precursor solution was sandwiched between a hydrophobic glass slide, treated with Sigmacote (Millipore), and a silanized 15 mm glass coverslip, and polymerization was performed in a vacuum chamber for 45 min. Next, 1 ml of 0.05 mg ml^{-1} type I collagen (rat tail collagen, Santa Cruz Biotechnology) was added onto the UV-sterilized PAaf gels and incubated either overnight at 4°C or 30 min at 37°C. To investigate the fidelity of the PAaf gels for epithelial monolayer formation on very soft gel, pristine PA gels of the composition, 4% A:0.075% B, were fabricated. Prior to addition of collagen solution, the pristine PA gels were functionalized with a UV-activated heterobifunctional crosslinker (Sulfo-SANPAH, Pierce, USA; 0.5 mg/ml in 50 mM HEPES, pH 8.5) under UV exposure (365 nm) for 10 min as described elsewhere (Fischer et al., 2012).

Mechanical characterization of PAaf gels

Mechanical characterization of PA gels was performed using an MFP-3D-BIO atomic force microscope (AFM, Asylum Research, Santa Barbara, CA, USA). Olympus TR400PB AFM probes with an Au/Cr-coated silicon nitride cantilever and pyramidal tip were used. Measurements were acquired by indenting the gels using the AFM probe with spring constants of 20–30 pN/nm, as measured by thermal calibration. Elastic moduli were analyzed from force curves using a modified Hertz model (Mackay and Kumar, 2013).

Force spectroscopy of collagen tethering

The properties of short and long collagen fiber tethering to the PAaf gels of varying stiffness were investigated by AFM-based force spectroscopy. For this experiment, Olympus TR400PB AFM probes with an Au/Cr-coated silicon nitride cantilevers with pyramidal tip were functionalized with an anti-collagen-I antibody using previously established methods (Fuhrmann et al., 2008; Wen et al., 2014). Briefly, cantilevers were cleaned with chloroform (Cambridge Isotope Laboratories) for 30 s and treated overnight with 5 M ethanolamine-hydrochloride (Chem-Impex International; dissolved in DMSO) at room temperature. Cantilevers were rinsed with PBS and subsequently treated with 25 mM bis(sulfosuccinimidyl) suberate (BS2; Pierce) for 30 min at room temperature. After washing with PBS, cantilevers were immersed in an anti-collagen-I antibody at concentration of 200 µg/ml (Sigma-Aldrich, C2456, 029M4762V) for 30 min at room temperature. Anti-collagen-I antibody-functionalized cantilevers were rinsed with PBS, dried and kept at 4°C until use. Measurements were taken on the collagen-coated PAaf gels (placed in PBS) in a regular 10×10 array of points spaced 10 µm apart using the functionalized cantilever at the speed of 2 µm/s. A dwell time of 1 s was introduced between approach and retraction cycles to facilitate binding of the antibody to collagen fiber. The generated deflection versus z-sensor position force curves were converted to force versus piezo displacement (Fig. S5B), and the number of ruptures, collagen fiber stiffness, rupture force and length were analyzed using a previously described method (Fuhrmann et al., 2008).

Fluorescent labeling of collagen and imaging

To visualize collagen coated onto polyacrylamide hydrogel, we fluorescently labeled collagen I with a slight modification of previously described method (Doyle et al., 2015). Briefly, 1.5 ml of a 3 mg ml^{-1} collagen I solution (pH ∼7.5) was gelled at 37°C in a well of a 12-multiwell plate and incubated with 0.2 M sodium bicarbonate buffer (pH 9.0, Sigma-Aldrich) for 10 min. Then the gel was incubated with 500 µl of Sulfo-Cyanine5 NHS ester dye (Lumiprobe Co. USA, 13320, RD77C) solution (dissolved in DMSO) at room temperature in the dark for 1 h. To quench the remaining NHS ester, 3 ml of 50 mM Tris-HCl buffer (pH 7.5, Sigma-Aldrich) was added to the gel. The stained collagen gel was washed six times with PBS over 2 h and 200 mM HCl (Sigma-Aldrich) was added to solubilize the collagen gel. The collagen solution was dialyzed against 20 mM acetic acid (Sigma-Aldrich) at a ratio of 1:1000 (protein solution:dialysis buffer) with continuous stirring at 4°C for 4 h using a 10,000 MWCO dialysis cassette (Thermo Fisher Scientific). To prepare the working collagen solution, 4% of the unlabeled collagen I solution (25, 50 and 100 µg/ml) was removed and replaced with same amount of fluorescently labeled collagen I solution. The collagen-coated PAaf hydrogels were imaged using a Zeiss LSM 880 laser-scanning confocal microscope (Carl Zeiss Microscopy, Germany). MATLAB supported CT-FIRE was used to measure collagen fiber length, alignment and straightness automatically from the confocal images as reported elsewhere (Bredfeldt et al., 2014).

Cell colony seeding and culture

After incubation for certain time and at certain temperature, collagen solution was aspirated and the gels were washed three times with sterile phosphate-buffered saline (PBS). Prior to seeding cells, the surface of the gel was air dried for 30 min to facilitate cell colony seeding. To create a small cell colony, MCF10A cells (provided by the Tissue Culture Support Center, Washington University, St Louis, USA) were seeded onto the middle of the gel by putting a tiny droplet of 5 µl cell suspension containing 50,000 cells. Cells were cultured in DMEM/F12 (Invitrogen) supplemented with 5% (v/v) horse serum (Invitrogen), 20 ng/ml epidermal growth factor (EGF, Miltenyi Biotec Inc), 0.5 mg/ml hydrocortisone (Sigma-Aldrich), 100 ng/ml cholera toxin (Sigma-Aldrich), 10 µg/ml insulin (Sigma-Aldrich) and 1% (v/v) penicillin-streptomycin (Sigma-Aldrich). To understand the efficiency of homogenous cell attachment to the surface of the PA gels, multiple phase-contrast images (10× magnification objective) of the epithelial cell monolayer were acquired using a tile function of ZEN program of a Zeiss AxioObserver Z1 microscope covering a wide area (9 mm×5 mm). A single image was generated by stitching the tile images using ImageJ (National Institutes of Health).

To investigate the effect of Rac1 on finger-like cell streaming, the Rac GTPase inhibitor NSC23766 (Santa Cruz Biotechnology) was added to the cell culture medium at the final concentration of 20 µM at least 16 h after cell seeding once the cell monolayer formed. After adding the drug, the cell monolayer was tracked for the next 24 h using time-lapse microscope.

To understand the influence of junctional E-cadherin on multicellular stream formation, cell–cell junctions were disrupted with the Ca^{2+} chelator EGTA (Sigma-Aldrich) according to previous studies (Nasrollahi et al., 2017; Tambe et al., 2011). Cells were incubated with EGTA (4 mM) after 12 h of seeding and imaged for the next 12 h through time-lapse microscopy at 30-min intervals.

Time-lapse microscopy and phase-contrast image analysis

Phase-contrast live-cell imaging was performed using a Zeiss AxioObserver Z1 microscope (Carl Zeiss Microscopy) equipped with an incubation chamber. In each experiment, phase-contrast images were acquired every 30 min over a 48 h period using a 10× objective. The number of multicellular streams and protrusion blebs, and their dimensions, were analyzed after 36 h of cell seeding in all conditions. The length and width of the protruding structures and number of cells beyond the baseline were measured manually with ImageJ. The width of the stream was calculated as an average of measured values at three random locations of the stream. Using ImageJ, cells were manually outlined and the cell area and aspect ratio (fit into an ellipse) were measured for at least 100 cells per condition.

Particle image velocimetry

Particle image velocimetry (PIV) analysis was performed to calculate spatiotemporal profiles of velocity magnitudes through PIVlab package in MATLAB (Thielicke and Stamhuis, 2014). PIV was run for three passes of 64-, 32- and 16-pixel windows to obtain the velocity field (v_i). To calculate cell alignment, the order parameter, defined as the cosine of the angle between the velocity vector at a given point and the principal velocity vector, was calculated. The principal velocity vector for a monolayer was calculated as the vector sum of all velocity vectors inside the monolayer. For a stream, the principal vector was calculated along the longest median of the triangle used to fit the region occupied by the stream (Fig. S3B). To quantify cell–cell coordination, velocity correlation lengths (E) were calculated. First, an

Journal of Cell Science (2019) 132, jcs226753. doi:10.1242/jcs.226753

autocorrelation function, $C(\rho)$ was computed by averaging the correlation coefficients over all directions:

$$C(\rho) = \frac{\sum_{ij}((v_i.v_j)/(||v_i||||v_j||))\delta(\rho - d_{ij})}{\sum_{ij}\delta(\rho - d_{ij})}$$

$$\delta(x) = \begin{cases} 1, & \text{if } 0 \le x < w \\ 0, & \text{otherwise} \end{cases}$$

Here, ρ represents the distance from index position, d_{ij} is the distance between the two positions (ith and jth), and w is the width of annulus within which correlation is calculated. $C(\rho)$ was then plotted as a function of ρ. In addition, the correlation length (E) was defined as the slope of the negative exponential used to fit $C(\rho)$, as shown in Fig. S3A. Order parameter, correlation length and kymograph analyses were performed using custom MATLAB codes (available from the corresponding author upon request).

Fourier-transform traction microscopy

Gel deformations were measured from fluorescent marker beads (0.2 µm) embedded inside the gels. Fluorescent beads near the top surface of the gel (<10 µm depth) were imaged using confocal microscopy. Next, cells were detached from the gels using trypsin (10×) and subsequently these beads were imaged again to get the reference image. To correct for stage drift, we matched fluorescent beads in unstrained parts of the gels between the first and the reference image. Experiments were conducted in 37°C and 5% CO_2 on a confocal microscope with a 10× magnification objective. Bead displacements were calculated using PIV. These displacements were then used to calculate tractions using the algorithm reported previously (Trepat et al., 2009), which is non-regularized and takes into account the force imbalance in finitely thick substrates. The algorithm was implemented in MATLAB.

Monolayer stress microscopy

Intercellular stresses were calculated from the traction forces with a previously described algorithm (Tambe et al., 2011, 2013). Briefly, a finite element analysis (FEA) scheme was used to model the cell monolayer, which was assumed to behave as a thin sheet of uniform thickness (Poisson's ratio 0.5, 5 µm height and Young's modulus of 10 kPa). The problem was reduced to a boundary value problem where the scalar potential was minimized with respect to displacements (u). The potential per unit thickness is described as follows:

$$\Pi = \iint_{\Omega} \frac{1}{2}\sigma_{ij}\varepsilon_{ij}dA - \int_{\tau} u_j T_j dS,$$

where ε_{ij} is plain strain and σ_{ij} is plane stress tensor. u_j and T_j represent the displacement and traction field. τ and Ω represent finite element edge and area respectively. Upon minimization, the problem was reduced to matrix form: $Ku=f$, where u and f are nodal displacement and force and K the global stiffness matrix. First displacements (u_j) are obtained by solving the above linear equations. Displacements are then used to calculate stresses (σ_{ij}) using constitutive equations assuming material linearity. The obtained stresses were decomposed into principal components (σ_{max} and σ_{min}) to obtain average normal stress $\left(\frac{\sigma_{max}+\sigma_{min}}{2}\right)$ and maximum shear stress $\left(\frac{\sigma_{max}-\sigma_{min}}{2}\right)$. The FEA grid was made up of four node square elements of side equal to 6.5 µm and matched the traction grid.

Boundary conditions at the leading edge was assumed to be stress free ($\sigma_{ij}n_i=0$). At the optical edges, normal displacements and shear stresses were assigned as zero ($u_in_i=0$, $\sigma_{ij}n_jt_i=0$). FEA scheme was implemented in MATLAB.

Immunofluorescence, confocal microscopy and image analysis

After 2 days of culturing, cells were fixed with 4% paraformaldehyde in PBS, followed by the addition of 0.1% Triton-X 100 (Sigma-Aldrich) for permeabilization of the cell membrane and blocking with 2% BSA in PBS. Primary antibody labeling was performed in 0.5% BSA in PBS overnight at 4°C with rabbit monoclonal anti-YAP (Cell Signaling Technology; 1:200 dilution, 14074S), rabbit monoclonal anti-vimentin (Cell Signaling Technology; diluted 1:200, 5741S) and mouse monoclonal anti-E-cadherin (Cell Signaling Technology; 1:400 dilution, 14472S) antibodies in separate experiments. Secondary antibody labeling was performed using the same procedure with Alexa Fluor 488-labeled goat anti-rabbit-IgG (Cell Signaling Technology; 1:500 dilution, 4412S), Alexa Fluor 647-labeled goat anti-rabbit-IgG (Cell Signaling Technology; 1:500 dilution, 4414S) and Alexa Fluor 488-labeled goat anti-mouse-IgG (Cell Signaling Technology; 1:500 dilution, 4408S) in separate experiments. Nuclei and F-actin staining was performed with 4′,6-diamidino-2-phenylindole (DAPI, Santa Cruz Biotechnology; 1:500 dilution, sc-3598) and Rhodamine–phalloidin (Invitrogen; 1:200 dilution, R415, 1888567), respectively. Confocal microscopy was performed using a Zeiss LSM 880 confocal microscope (Carl Zeiss Microscopy); z-stacks were acquired at 1 µm interval and combined with the Z-projection tool in ImageJ using the maximum intensity setting. All images were taken using same acquisition parameters including laser power, scan speed and pixel resolution, to ensure accurate quantitative image analysis. Vimentin expression was analyzed from at least ten field of views from three independent experiments and the expression level was computed by measuring integrated fluorescence intensity and normalized to the cell number. Cell number was computed by using the automatic cell counting tool of ImageJ. To quantify the subcellular YAP activity, the mean fluorescence intensity of YAP was measured in the nucleus and the cytoplasm by selecting regions of interest (ROIs). Nuclear YAP localization was calculated from the ratio of nuclear to cytoplasmic YAP intensity of at least 100 cells from randomly selected 10 to 15 field of views of three independent experiments. F-actin intensity was analyzed by measuring the integrated fluorescence intensity in ROIs after subtracting the background signals and presented per unit area of ROI.

Western blotting

After 2 days of culture, wild-type and Rac1-inhibited cells were lysed in RIPA buffer supplemented with phenylmethylsulfonyl fluoride (PMSF), sodium orthovanadate and protease inhibitor cocktail supplied by Santa Cruz Biotechnology. The lysates were centrifuged at 6500 ***g*** at 4°C for 20 min and supernatants were collected. The concentrations for the total protein concentrations were quantified by Bradford assay (Thermo Fisher Scientific). Equal amounts of protein were mixed with LDS sample buffer (Bolt™; Invitrogen) and reducing agent (Bolt™; Invitrogen) and heated at 95°C for 5 min and stored at −20°C until further use. Proteins were separated on 4–12% Bis-Tris Plus Gels (Bolt™; Invitrogen) using 1× MES running buffer at a constant voltage (200 V) for 22 min. The protein bands were transferred to a nitrocellulose membrane using a semi-dry blotting system, iBlot™ 2 Gel Transfer Device (Invitrogen). Antibody conjugation was performed with a primary antibodies [rabbit monoclonal vimentin (1:1000; Cell Signaling Technology, 5741), rabbit monoclonal E-cadherin (1:1000; Cell Signaling Technology, 3195), and rabbit monoclonal α-Tubulin (1:1000; Cell Signaling Technology, 2144)] followed by secondary antibody [IRDye® 800CW goat anti-Rabbit IgG (1:5000; LI-COR Biotechnology, 926-32211, C81210-05)] for 2 h at room temperature using a iBind™ Western Device (Invitrogen). Membrane was imaged using an Odyssey® CLX system (LI-COR Biotechnology).

Scanning electron microscopy

PAaf gels were made as described above, except that 25 µl of gel precursor solution was polymerized between a hydrophobic glass slide and a 12 mm silanized glass coverslip. After collagen coating at the specific conditions, as described above, the gel substrates were fixed in the mixture of freshly prepared 2.5% glutaraldehyde and 2% paraformaldehyde in 0.1 M cacodylate buffer with 2 mM calcium chloride for overnight at 4°C. The gels were rinsed three times in 0.1 M cacodylate buffer with 2 mM calcium chloride for 10 min each time. Secondary fixation was performed in 1% osmium tetroxide in 0.1 M cacodylate buffer for 1 h in dark. Next, the gels were rinsed three times in ultrapure water (Direct-Q, Merck Millipore) for 10 min each time and subsequently dehydrated in a graded ethanol series (50, 70, 80, 90 and 99.8%). The samples were dried with a critical point dryer (Leica EM CPD300) and coated with approximately 10 nm of iridium (Leica, ACE 600) before acquiring images using a high-resolution scanning electron microscope (SEM), Zeiss Merlin FE-SEM.

Statistical analysis

Data are presented as the mean±s.e.m. Statistical significance was computed by one-way analysis of variance (ANOVA). The pairwise comparison of the means was calculated with a Bonferroni's test (post-hoc comparison). Differences were considered as statistically significant for $P<0.05$.

Acknowledgements

Scanning electron microscopy was performed through the use of Washington University Center for Cellular Imaging (WUCCI).

Competing interests

The authors declare no competing or financial interests.

Author contributions

Conceptualization: B.S., A.B., A.P.; Methodology: B.S., A.B., C.W., J.A., A.P.; Software: A.B., A.P.; Validation: B.S., A.B., C.W., J.A., A.P.; Formal analysis: B.S., A.B., C.W., J.A., A.P.; Investigation: B.S., A.B., A.P.; Resources: A.P.; Data curation: B.S., A.B., A.P.; Writing - original draft: B.S., A.B., A.P.; Writing - review & editing: A.P.; Visualization: B.S., A.B., A.P.; Supervision: A.P.; Project administration: A.P.; Funding acquisition: A.P.

Funding

This work was supported in part by the National Institutes of Health (R35 GM128764) grant to A.P. Deposited in PMC for release after 12 months.

Supplementary information

Supplementary information available online at
http://jcs.biologists.org/lookup/doi/10.1242/jcs.226753.supplemental

References

Bredfeldt, J. S., Liu, Y., Pehlke, C. A., Conklin, M. W., Szulczewski, J. M., Inman, D. R., Keely, P. J., Nowak, R. D., Mackie, T. R. and Eliceiri, K. W. (2014). Computational segmentation of collagen fibers from second-harmonic generation images of breast cancer. *J. Biomed. Opt.* **19**, 016007. doi:10.1117/1.JBO.19.1.016007

Brown, A. C., Fiore, V. F., Sulchek, T. A. and Barker, T. H. (2013). Physical and chemical microenvironmental cues orthogonally control the degree and duration of fibrosis-associated epithelial-to-mesenchymal transitions. *J. Pathol.* **229**, 25-35. doi:10.1002/path.4114

Cheung, K. J., Gabrielson, E., Werb, Z. and Ewald, A. J. (2013). Collective invasion in breast cancer requires a conserved basal epithelial program. *Cell* **155**, 1639-1651. doi:10.1016/j.cell.2013.11.029

Cheung, K. J., Padmanaban, V., Silvestri, V., Schipper, K., Cohen, J. D., Fairchild, A. N., Gorin, M. A., Verdone, J. E., Pienta, K. J., Bader, J. S. et al. (2016). Polyclonal breast cancer metastases arise from collective dissemination of keratin 14-expressing tumor cell clusters. *Proc. Natl. Acad. Sci. USA* **113**, E854-E863. doi:10.1073/pnas.1508541113

Clark, A. G. and Vignjevic, D. M. (2015). Modes of cancer cell invasion and the role of the microenvironment. *Curr. Opin. Cell Biol.* **36**, 13-22. doi:10.1016/j.ceb.2015.06.004

Corey, E. J. and Suggs, J. W. (1975). Pyridinium chlorochromate. An efficient reagent for oxidation of primary and secondary alcohols to carbonyl compounds. *Tetrahedron Lett.* **16**, 2647-2650. doi:10.1016/S0040-4039(00)75204-X

Dang, T. T., Prechtl, A. M. and Pearson, G. W. (2011). Breast cancer subtype-specific interactions with the microenvironment dictate mechanisms of invasion. *Cancer Res.* **71**, 6857. doi:10.1158/0008-5472.CAN-11-1818

Dingal, P. C. D. P., Bradshaw, A. M., Cho, S., Raab, M., Buxboim, A., Swift, J. and Discher, D. E. (2015). Fractal heterogeneity in minimal matrix models of scars modulates stiff-niche stem-cell responses via nuclear exit of a mechanorepressor. *Nat. Mater.* **14**, 951. doi:10.1038/nmat4350

Discher, D. E., Janmey, P. and Wang, Y.-L. (2005). Tissue cells feel and respond to the stiffness of their substrate. *Science* **310**, 1139-1143. doi:10.1126/science.1116995

Doyle, A. D., Carvajal, N., Jin, A., Matsumoto, K. and Yamada, K. M. (2015). Local 3D matrix microenvironment regulates cell migration through spatiotemporal dynamics of contractility-dependent adhesions. *Nat. Commun.* **6**, 8720. doi:10.1038/ncomms9720

Dupont, S., Morsut, L., Aragona, M., Enzo, E., Giulitti, S., Cordenonsi, M., Zanconato, F., Le Digabel, J., Forcato, M., Bicciato, S. et al. (2011). Role of YAP/TAZ in mechanotransduction. *Nature* **474**, 179-183. doi:10.1038/nature10137

Ehrlich, J. S., Hansen, M. D. H. and Nelson, W. J. (2002). Spatio-temporal regulation of Rac1 localization and lamellipodia dynamics during epithelial cell-cell adhesion. *Dev. Cell* **3**, 259-270. doi:10.1016/S1534-5807(02)00216-2

Elkhatib, N., Bresteau, E., Baschieri, F., Rioja, A. L., van Niel, G., Vassilopoulos, S. and Montagnac, G. (2017). Tubular clathrin/AP-2 lattices pinch collagen fibers to support 3D cell migration. *Science* **356**, eaal4713. doi:10.1126/science.aal4713

Elliott, J. T., Tona, A., Woodward, J. T., Jones, P. L. and Plant, A. L. (2003). Thin films of collagen affect smooth muscle cell morphology. *Langmuir* **19**, 1506-1514. doi:10.1021/la026216r

Elosegui-Artola, A., Andreu, I., Beedle, A. E. M., Lezamiz, A., Uroz, M., Kosmalska, A. J., Oria, R., Kechagia, J. Z., Rico-Lastres, P., Le Roux, A.-L. et al. (2017). Force triggers YAP nuclear entry by regulating transport across nuclear pores. *Cell* **171**, 1397-1410.e14. doi:10.1016/j.cell.2017.10.008

Engler, A. J., Sen, S., Sweeney, H. L. and Discher, D. E. (2006). Matrix elasticity directs stem cell lineage specification. *Cell* **126**, 677-689. doi:10.1016/j.cell.2006.06.044

Fischer, R. S., Myers, K. A., Gardel, M. L. and Waterman, C. M. (2012). Stiffness-controlled three-dimensional extracellular matrices for high-resolution imaging of cell behavior. *Nat. Protoc.* **7**, 2056-2066. doi:10.1038/nprot.2012.127

Friedl, P. and Gilmour, D. (2009). Collective cell migration in morphogenesis, regeneration and cancer. *Nat. Rev. Mol. Cell Biol.* **10**, 445-457. doi:10.1038/nrm2720

Fuhrmann, A., Anselmetti, D., Ros, R., Getfert, S. and Reimann, P. (2008). Refined procedure of evaluating experimental single-molecule force spectroscopy data. *Phys. Rev. E* **77**, 031912. doi:10.1103/PhysRevE.77.031912

Gaggioli, C., Hooper, S., Hidalgo-Carcedo, C., Grosse, R., Marshall, J. F., Harrington, K. and Sahai, E. (2007). Fibroblast-led collective invasion of carcinoma cells with differing roles for RhoGTPases in leading and following cells. *Nat. Cell Biol.* **9**, 1392-1400. doi:10.1038/ncb1658

Gurry, T., Nerenberg, P. S. and Stultz, C. M. (2010). The contribution of interchain salt bridges to triple-helical stability in collagen. *Biophys. J.* **98**, 2634-2643. doi:10.1016/j.bpj.2010.01.065

Han, W., Chen, S., Yuan, W., Fan, Q., Tian, J., Wang, X., Chen, L., Zhang, X., Wei, W., Liu, R. et al. (2016). Oriented collagen fibers direct tumor cell intravasation. *Proc. Natl Acad. Sci. USA* **113**, 11208-11213. doi:10.1073/pnas.1610347113

Lee, K. A., Chen, Q. K., Lui, C., Cichon, M. A., Radisky, D. C. and Nelson, C. M. (2012). Matrix compliance regulates Rac1b localization, NADPH oxidase assembly, and epithelial-mesenchymal transition. *Mol. Biol. Cell* **23**, 4097-4108. doi:10.1091/mbc.e12-02-0166

Lee, J. P., Kassianidou, E., MacDonald, J. I., Francis, M. B. and Kumar, S. (2016). N-terminal specific conjugation of extracellular matrix proteins to 2-pyridinecarboxaldehyde functionalized polyacrylamide hydrogels. *Biomaterials* **102**, 268-276. doi:10.1016/j.biomaterials.2016.06.022

Leight, J. L., Wozniak, M. A., Chen, S., Lynch, M. L. and Chen, C. S. (2012). Matrix rigidity regulates a switch between TGF-beta1-induced apoptosis and epithelial-mesenchymal transition. *Mol. Biol. Cell* **23**, 781-791. doi:10.1091/mbc.e11-06-0537

Leung, E., Xue, A., Wang, Y., Rougerie, P., Sharma, V. P., Eddy, R., Cox, D. and Condeelis, J. (2017). Blood vessel endothelium-directed tumor cell streaming in breast tumors requires the HGF/C-Met signaling pathway. *Oncogene* **36**, 2680-2692. doi:10.1038/onc.2016.421

Mack, N. A., Whalley, H. J., Castillo-Lluva, S. and Malliri, A. (2011). The diverse roles of Rac signaling in tumorigenesis. *Cell Cycle* **10**, 1571-1581. doi:10.4161/cc.10.10.15612

Mackay, J. L. and Kumar, S. (2013). Measuring the elastic properties of living cells with atomic force microscopy indentation. *Methods Mol. Biol.* **931**, 313-329. doi:10.1007/978-1-62703-056-4_15

Mayor, R. and Etienne-Manneville, S. (2016). The front and rear of collective cell migration. *Nat. Rev. Mol. Cell Biol.* **17**, 97. doi:10.1038/nrm.2015.14

McDaniel, D. P., Shaw, G. A., Elliott, J. T., Bhadriraju, K., Meuse, C., Chung, K.-H. and Plant, A. L. (2007). The stiffness of collagen fibrils influences vascular smooth muscle cell phenotype. *Biophys. J.* **92**, 1759-1769. doi:10.1529/biophysj.106.089003

Mouw, J. K., Ou, G. and Weaver, V. M. (2014). Extracellular matrix assembly: a multiscale deconstruction. *Nat. Rev. Mol. Cell Biol.* **15**, 771-785. doi:10.1038/nrm3902

Nasrollahi, S. and Pathak, A. (2016). Topographic confinement of epithelial clusters induces epithelial-to-mesenchymal transition in compliant matrices. *Sci. Rep.* **6**, 18831. doi:10.1038/srep18831

Nasrollahi, S. and Pathak, A. (2017). Hydrogel-based microchannels to measure confinement- and stiffness-sensitive Yes-associated-protein activity in epithelial clusters. *MRS Communications* **7**, 450-457. doi:10.1557/mrc.2017.87

Nasrollahi, S., Walter, C., Loza, A. J., Schimizzi, G. V., Longmore, G. D. and Pathak, A. (2017). Past matrix stiffness primes epithelial cells and regulates their future collective migration through a mechanical memory. *Biomaterials* **146**, 146-155. doi:10.1016/j.biomaterials.2017.09.012

Omelchenko, T., Vasiliev, J. M., Gelfand, I. M., Feder, H. H. and Bonder, E. M. (2003). Rho-dependent formation of epithelial "leader" cells during wound healing. *Proc. Natl Acad. Sci. USA* **100**, 10788. doi:10.1073/pnas.1834401100

Pathak, A. (2016). Scattering of cell clusters in confinement. *Biophys. J.* **111**, 1496-1506. doi:10.1016/j.bpj.2016.08.034

Pelham, R. J. and Wang, Y.-L. (1997). Cell locomotion and focal adhesions are regulated by substrate flexibility. *Proc. Natl. Acad. Sci. USA* **94**, 13661-13665. doi:10.1073/pnas.94.25.13661

Persikov, A. V., Ramshaw, J. A. M., Kirkpatrick, A. and Brodsky, B. (2005). Electrostatic interactions involving lysine make major contributions to collagen triple-helix stability. *Biochemistry* **44**, 1414-1422. doi:10.1021/bi048216r

Poujade, M., Grasland-Mongrain, E., Hertzog, A., Jouanneau, J., Chavrier, P., Ladoux, B., Buguin, A. and Silberzan, P. (2007). Collective migration of an epithelial monolayer in response to a model wound. *Proc. Natl Acad. Sci. USA* **104**, 15988. doi:10.1073/pnas.0705062104

Reffay, M., Petitjean, L., Coscoy, S., Grasland-Mongrain, E., Amblard, F., Buguin, A. and Silberzan, P. (2011). Orientation and polarity in collectively migrating cell structures: statics and dynamics. *Biophys. J.* **100**, 2566-2575. doi:10.1016/j.bpj.2011.04.047

Reffay, M., Parrini, M. C., Cochet-Escartin, O., Ladoux, B., Buguin, A., Coscoy, S., Amblard, F., Camonis, J. and Silberzan, P. (2014). Interplay of RhoA and mechanical forces in collective cell migration driven by leader cells. *Nat. Cell Biol.* **16**, 217-223. doi:10.1038/ncb2917

Riching, K. M., Cox, B. L., Salick, M. R., Pehlke, C., Riching, A. S., Ponik, S. M., Bass, B. R., Crone, W. C., Jiang, Y., Weaver, A. M. et al. (2014). 3D collagen alignment limits protrusions to enhance breast cancer cell persistence. *Biophys. J.* **107**, 2546-2558. doi:10.1016/j.bpj.2014.10.035

Rottner, K. and Stradal, T. E. B. (2011). Actin dynamics and turnover in cell motility. *Curr. Opin. Cell Biol.* **23**, 569-578. doi:10.1016/j.ceb.2011.07.003

Saha, K., Keung, A. J., Irwin, E. F., Li, Y., Little, L., Schaffer, D. V. and Healy, K. E. (2008). Substrate modulus directs neural stem cell behavior. *Biophys. J.* **95**, 4426-4438. doi:10.1529/biophysj.108.132217

Sarker, B., Papageorgiou, D. G., Silva, R., Zehnder, T., Gul-E-Noor, F., Bertmer, M., Kaschta, J., Chrissafis, K., Detsch, R. and Boccaccini, A. R. (2014). Fabrication of alginate–gelatin crosslinked hydrogel microcapsules and evaluation of the microstructure and physico-chemical properties. *J. Mater. Chem. B* **2**, 1470. doi:10.1039/c3tb21509a

Sharma, P., Ng, C., Jana, A., Padhi, A., Szymanski, P., Lee, J. S. H., Behkam, B., Nain, A. S. and Blanchoin, L. (2017). Aligned fibers direct collective cell migration to engineer closing and nonclosing wound gaps. *Mol. Biol. Cell* **28**, 2579-2588. doi:10.1091/mbc.e17-05-0305

Sunyer, R., Conte, V., Escribano, J., Elosegui-Artola, A., Labernadie, A., Valon, L., Navajas, D., García-Aznar, J. M., Muñoz, J. J., Roca-Cusachs, P. et al. (2016). Collective cell durotaxis emerges from long-range intercellular force transmission. *Science* **353**, 1157. doi:10.1126/science.aaf7119

Swartz, M. A., Iida, N., Roberts, E. W., Sangaletti, S., Wong, M. H., Yull, F. E., Coussens, L. M. and DeClerck, Y. A. (2012). Tumor microenvironment complexity: emerging roles in cancer therapy. *Cancer Res.* **72**, 2473-2480. doi:10.1158/0008-5472.CAN-12-0122

Tambe, D. T., Corey Hardin, C., Angelini, T. E., Rajendran, K., Park, C. Y., Serra-Picamal, X., Zhou, E. H., Zaman, M. H., Butler, J. P., Weitz, D. A. et al. (2011). Collective cell guidance by cooperative intercellular forces. *Nat. Mater.* **10**, 469-475. doi:10.1038/nmat3025

Tambe, D. T., Croutelle, U., Trepat, X., Park, C. Y., Kim, J. H., Millet, E., Butler, J. P. and Fredberg, J. J. (2013). Monolayer stress microscopy: limitations, artifacts, and accuracy of recovered intercellular stresses. *PLoS ONE* **8**, e55172. doi:10.1371/journal.pone.0055172

Thielicke, W. and Stamhuis, E. J. (2014). PIVlab – towards user-friendly, affordable and accurate digital particle image velocimetry in MATLAB. *J. Open Res. Softw.* **2**, e30. doi:10.5334/jors.bl

Trepat, X., Wasserman, M. R., Angelini, T. E., Millet, E., Weitz, D. A., Butler, J. P. and Fredberg, J. J. (2009). Physical forces during collective cell migration. *Nat. Phys.* **5**, 426-430. doi:10.1038/nphys1269

Ulrich, T. A., De Juan Pardo, E. M. and Kumar, S. (2009). The mechanical rigidity of the extracellular matrix regulates the structure, motility, and proliferation of glioma cells. *Cancer Res.* **69**, 4167-4174. doi:10.1158/0008-5472.CAN-08-4859

Walter, C., Davis, J. T., Mathur, J. and Pathak, A. (2018). Physical defects in basement membrane-mimicking collagen-IV matrices trigger cellular EMT and invasion. *Integr. Biol.* **10**, 342-355. doi:10.1039/c8ib00034d

Wei, S. C., Fattet, L., Tsai, J. H., Guo, Y., Pai, V. H., Majeski, H. E., Chen, A. C., Sah, R. L., Taylor, S. S., Engler, A. J. et al. (2015). Matrix stiffness drives epithelial-mesenchymal transition and tumour metastasis through a TWIST1-G3BP2 mechanotransduction pathway. *Nat. Cell Biol.* **17**, 678-688. doi:10.1038/ncb3157

Wen, J. H., Vincent, L. G., Fuhrmann, A., Choi, Y. S., Hribar, K. C., Taylor-Weiner, H., Chen, S. and Engler, A. J. (2014). Interplay of matrix stiffness and protein tethering in stem cell differentiation. *Nat. Mater.* **13**, 979-987. doi:10.1038/nmat4051

Wirtz, D., Konstantopoulos, K. and Searson, P. C. (2011). The physics of cancer: the role of physical interactions and mechanical forces in metastasis. *Nat. Rev. Cancer* **11**, 512-522. doi:10.1038/nrc3080

Yamaguchi, N., Mizutani, T., Kawabata, K. and Haga, H. (2015). Leader cells regulate collective cell migration via Rac activation in the downstream signaling of integrin beta1 and PI3K. *Sci. Rep.* **5**, 7656. doi:10.1038/srep07656

Zaman, M. H., Trapani, L. M., Sieminski, A. L., Siemeski, A., Mackellar, D., Gong, H., Kamm, R. D., Wells, A., Lauffenburger, D. A. and Matsudaira, P. (2006). Migration of tumor cells in 3D matrices is governed by matrix stiffness along with cell-matrix adhesion and proteolysis. *Proc. Natl. Acad. Sci. USA* **103**, 10889-10894. doi:10.1073/pnas.0604460103

Zhao, B., Wei, X., Li, W., Udan, R. S., Yang, Q., Kim, J., Xie, J., Ikenoue, T., Yu, J., Li, L. et al. (2007). Inactivation of YAP oncoprotein by the Hippo pathway is involved in cell contact inhibition and tissue growth control. *Genes Dev.* **21**, 2747-2761. doi:10.1101/gad.1602907

Zorn, M. L., Marel, A.-K., Segerer, F. J. and Rädler, J. O. (2015). Phenomenological approaches to collective behavior in epithelial cell migration. *Biochim. Biophys. Acta Mol. Cell Res.* **1853**, 3143-3152. doi:10.1016/j.bbamcr.2015.05.021